

Three-dimensional flow structures and vorticity control in fish-like swimming

By Q. ZHU, M. J. WOLFGANG†, D. K. P. YUE
AND M. S. TRIANTAFYLLOU‡

Department of Ocean Engineering, Massachusetts Institute of Technology,
Cambridge, MA 02139, USA

(Received 17 March 2000 and in revised form 8 April 2002)

We employ a three-dimensional, nonlinear inviscid numerical method, in conjunction with experimental data from live fish and from a fish-like robotic mechanism, to establish the three-dimensional features of the flow around a fish-like body swimming in a straight line, and to identify the principal mechanisms of vorticity control employed in fish-like swimming. The computations contain no structural model for the fish and hence no recoil correction. First, we show the near-body flow structure produced by the travelling-wave undulations of the bodies of a tuna and a giant danio. As revealed in cross-sectional planes, for tuna the flow contains dominant features resembling the flow around a two-dimensional oscillating plate over most of the length of the fish body. For the giant danio, on the other hand, a mixed longitudinal-transverse structure appears along the hind part of the body. We also investigate the interaction of the body-generated vortices with the oscillating caudal fin and with tail-generated vorticity. Two distinct vorticity interaction modes are identified: the first mode results in high thrust and is generated by constructive pairing of body-generated vorticity with same-sign tail-generated vorticity, resulting in the formation of a strong thrust wake; the second corresponds to high propulsive efficiency and is generated by destructive pairing of body-generated vorticity with opposite-sign tail-generated vorticity, resulting in the formation of a weak thrust wake.

1. Introduction

Fish locomotion offers a different paradigm of propulsion than utilized in human-engineered vehicles, employing a rhythmic unsteady motion of the body and fins. It has been shown in the literature that drag reduction and high propulsive efficiency are achievable through it. Gray (1936), in a still controversial paper, estimated that the drag on a swimming dolphin must be lower than on a towed rigid model of the dolphin body by a large factor; Lighthill (1971) used the kinematics measured in a live small fish, together with a large-amplitude slender body theory, and arrived at the opposite conclusion, i.e. that the drag on a swimming fish must be larger than on a rigidly towed fish model, by a factor of about three. Recently, precise measurements on an actively swimming robotic vehicle in the shape of a bluefin tuna show that the power needed to self-propel the robot is reduced by up to about 50% compared to the power needed to tow the robot straight-rigid (Barrett *et al.* 1999),

† Currently with The Boston Consulting Group, Inc., Boston, MA, USA.

‡ Author to whom correspondence should be addressed.

suggesting that the undulating motion of the swimming body leads to a smaller drag.

The efficiency of fish swimming has been illustrated in several studies. With slender body theory, Lighthill (1960, 1975) and Wu (1961, 1971*a, b, c*) obtained high efficiency in three-dimensional fish-like swimming. Using more realistic fish-like forms, however, numerical inviscid calculations by Cheng, Zhuang & Tong (1991) and Wolfgang (1999) show that slender body theory overpredicts thrust by a factor of up to 3 when the wavelength of imposed motion is roughly equal to the body length.

Closely related to the high performance of fish-like swimming, the near-field flow structure around a fish body has been studied both experimentally and computationally. Review papers (Pedley & Hill 1999; Triantafyllou, Triantafyllou & Yue 2000) present a summary of recent developments in numerical studies and visualization experiments. Whole-field velocimetry and numerical visualization have shed significant light on the details of the flow around the fish (Stamhuis & Videler 1995; Anderson 1996; Triantafyllou *et al.* 1996; Müller *et al.* 1997; Liu, Wassenberg & Kawachi 1997; Wolfgang *et al.* 1999*a*; Wolfgang, Triantafyllou & Yue 1999*b*). Among them, Anderson (1996) and Wolfgang *et al.* (1999*a, b*) illustrated the generation and manipulation of vorticity in a swimming and turning live fish. Liu *et al.* (1997) demonstrated, through CFD simulation of the swimming motion of a tadpole, the process of shedding body-bound vorticity through separation from the edges of the body near the tail and the wake consisting of counter-rotating and anti-symmetrically positioned three-dimensional vortical structures.

Body-bound vortices are created in front of the tail either from separation of the body boundary layer or the sharp edges of secondary fins or finlets. Earlier visualization work by Rosen (1959), using a narrow tank, shows free vortices forming well ahead of the peduncle and travelling along the body to reach the tail, where they are manipulated by the caudal fin and re-positioned in the wake. The role of these body-generated vortices in fish performance remains unclear. One unsolved question is whether they contribute directly to thrust production. The alternatives are that either the vorticity generated upstream from the peduncle is shed in an uncontrolled manner, much in the way a rigid hull ship does, generating a drag wake; or it is organized and shed in a controlled manner, such that the tail can manipulate it and optimize its performance. Considering the latter case, the tail operates within the oncoming shed vorticity, hence it is possible to enhance its performance through direct manipulation. For example, if the tail intercepts a vortex with its side inclined with respect to the oncoming flow such that it is upstream facing, it will generate thrust due to the low pressure associated with the vortex. Subsequently, though, the vortex must be repositioned to avoid the creation of a drag wake which results in an overall drag force.

In this study, we apply a panel method which is an extension of the numerical scheme described in Barrett *et al.* (1999) and Wolfgang *et al.* (1999*a*) to investigate flow structure and vorticity control in fish-like swimming. Employing this three-dimensional computational scheme, we first illustrate the complex three-dimensional details of the flow structure and wake near a fish, in order to correlate them with the swimming performance characteristics. With body geometry and kinematic parameters representing a tuna undergoing straight-line locomotion, the flow pattern is found to be mostly in the longitudinal direction along the whole length of the body, resembling the results of the two-dimensional swimming plate theory of Wu (1961). In the case of a giant danio (*Danio malabaricus*), on the other hand, the longitudinal pattern near the head is replaced by a mixture of longitudinal/transverse flow on moving closer to

the tail. Near the peduncle linking the body with the tail, the flow is more like that predicted by the three-dimensional slender body theory of Lighthill (1975).

The present work also addresses the issue of how the flow can be organized around the body so as to contribute to the overall performance; and what the basic mechanisms of vorticity control exerted by the tail are in order to recover energy or maximize thrust. Body-bound vortices are generated from the sharp trailing edges of the dorsal/ventral fins or finlets and interact with the tail and its wake. To establish vorticity control principles, we borrow from the developments in Gopalkrishnan *et al.* (1994) who studied mechanisms of controlling a vortical flow through an oscillating foil, and subsequent experiments by Anderson (1996) and Anderson *et al.* (1998) on the same problem, expanding the vorticity control mechanisms to include leading-edge vorticity from the foil. By investigating the interaction between the body-bound vorticity and the tail, two different modes of vorticity control are identified. In the first mode, the body-shed vorticity encounters the tail in a favourable manner, enforcing the tail-shed wake and increasing the thrust; in the second one, the body- and tail-generated wakes cancel each other to a certain extent, reducing the peak thrust somewhat, while increasing the propulsive efficiency.

The present paper is organized as follows. In §2, we present the physical problems, including the fish geometries, the kinematics of fish locomotion and the mathematical formulations. The development of the numerical method is given in §3. In §4, we conduct an investigation of the three-dimensional flow structures near a fish body during straight-line swimming. The vorticity control utilized in fish swimming is illustrated in §5. Finally, conclusions are drawn in §6.

2. Physical problem

We consider a streamlined flexible body of geometry S_b undergoing prescribed translating and angular motions as well as undulations about its mean line, with arbitrary distribution of sharp-trailing-edged fins, as detailed in figure 1. A thin shear layer wake S_w is shed from the sharp trailing edges continuously as time proceeds. With the exception of the wake, the fluid is assumed to be inviscid and irrotational, as well as incompressible, allowing the existence of a velocity potential $\Phi(\mathbf{x}, t)$.

We apply two coordinate systems in the study: an inertial global coordinate system $OXYZ$, fixed in space, and a local coordinate system $oxyz$, instantaneously fixed on the flexible body and orthonormal to the stretched-straight mean line and body section plane. The mean periodic undulations of the body is prescribed with reference to $oxyz$ and the global translational motion of the body is described with respect to $OXYZ$.

2.1. Mathematical formulation

We consider the fluid domain bounded by three surfaces: the body surface S_b , an infinitesimally thin wake sheet S_w , and a far-field boundary at infinity S_∞ . Assuming the flow to be inviscid and incompressible, for any point $\mathbf{x} = (X, Y, Z)$ within the fluid, the velocity could be described by a velocity potential $\Phi(\mathbf{x}, t)$ which satisfies Laplace's equation within the fluid, the no-flux condition on the surface of the body and a radiation condition such that $\Phi(\mathbf{x}, t)$ decays rapidly to zero in the far field.

The total potential $\Phi(\mathbf{x}, t)$ could be written as a linear superposition of a body perturbation velocity potential $\Phi_b(\mathbf{x}, t)$ and a wake perturbation velocity potential $\Phi_w(\mathbf{x}, t)$, each satisfying the Laplace field equation. The shear layers on wake surfaces

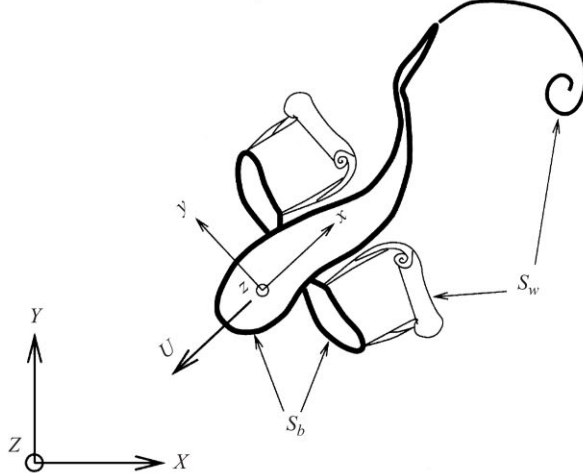


FIGURE 1. Coordinate system convention. $OXYZ$ is an inertial reference frame, while $oxyz$ is a body-fixed coordinate system about which mean line undulations are described.

S_w are represented by smoothly varying-strength dipole sheets. At any time, the dipole strength along the wake (with the exception of the most recently shed wake sheet) is determined by the previous flow field, and the wake perturbation velocity potential $\Phi_w(\mathbf{x}, t)$ is evaluated by summing the influence of all the wake dipoles. The unknown strength of the newest portion of the wake sheet is addressed through the unsteady Kutta condition which is applied to the sharp trailing edges of the body to enforce smooth flow leaving the body. Mathematically, at any time the strength of the shed wake velocity potential equals the jump in the body perturbation potential between the upper and lower surfaces near the trailing edge (for details, see Katz & Plotkin 1991). The rest of the wake follows the flow, thus the lengths of the shed wake surfaces increase with time.

We then formulate the boundary value problem for the body perturbation velocity potential $\Phi_b(\mathbf{x}, t)$. As described above, Φ_b satisfies the Laplace equation within the fluid and the radiation condition in the far field. The prescribed body motions $V_b(\mathbf{x}, t)$ and the induced velocities from the wake surfaces are used to find the normal velocity distribution on the body surface S_b . The no-flux kinematic boundary condition can be expressed as

$$\frac{\partial \Phi_b(\mathbf{x}, t)}{\partial \mathbf{n}} = \{V_b(\mathbf{x}, t) - \nabla \Phi_w(\mathbf{x}, t)\} \cdot \mathbf{n}, \quad (2.1)$$

where \mathbf{n} is the unit normal vector pointing out of the fluid. From Green's theorem, the body perturbation velocity potential $\Phi_b(\mathbf{x}, t)$ at any point can be described in terms of surface integrals over the body surface S_b , the wake sheet surface S_w and a boundary at infinity S_∞ . If this point \mathbf{x} is on the boundary, $\Phi_b(\mathbf{x}, t)$ satisfies the following equation:

$$-2\pi\Phi_b(\mathbf{x}, t) + \iint_S \Phi_b(\mathbf{x}', t) \frac{\partial(1/r)}{\partial n} d\mathbf{s}' = \iint_S \frac{1}{r} \frac{\partial \Phi_b(\mathbf{x}', t)}{\partial n} d\mathbf{s}', \quad (2.2)$$

where $S = S_b + S_w + S_\infty$, $r = |\mathbf{x} - \mathbf{x}'|$ is the distance from point $\mathbf{x}' \in S$ to the field point \mathbf{x} . Due to the nature of the singularities which appear as sources and dipoles in the integrands of (2.2), whose influence decays as $1/r$ and $1/r^2$, respectively, the boundary at infinity S_∞ can be shown to have negligible influence. Also, since both

the body potential Φ_b and its normal derivative are continuous across the wake, their contribution to the integrals over S_w in (2.2) should be zero.

At each time, with the wake position S_w and its strength Φ_w determined through time history, and the body perturbation potential Φ_b obtained by solving (2.2) with $\partial\Phi_b/\partial n$ on S_b given by (2.1), the total flow potential Φ and the hydrodynamic force \mathbf{F} are found by integrating the pressure p over the body surface S_b , which is determined by employing the unsteady Bernoulli equation. We have

$$\mathbf{F} = -\rho \iint_{S_b} \left(\frac{1}{2} \nabla \Phi \cdot \nabla \Phi + \frac{\partial \Phi}{\partial t} \right) \mathbf{n} ds', \quad (2.3)$$

where ρ is the density of the water. The power input P , defined as the rate of energy transmission to the fluid, is obtained as

$$P(t) = -\rho \iint_{S_b} \left(\frac{1}{2} \nabla \Phi \cdot \nabla \Phi + \frac{\partial \Phi}{\partial t} \right) \mathbf{V}_b \cdot \mathbf{n} ds'. \quad (2.4)$$

Finally, we define the propulsive efficiency for straight-line swimming η as

$$\eta = U \bar{F} / \bar{P}, \quad (2.5)$$

where U is the swimming speed, \bar{F} denotes the mean value of thrust and \bar{P} the mean power input.

2.2. Fish geometries

In the present work, we employ body shapes representing a tuna and a giant danio to study the flow structure around three-dimensional flexible bodies undergoing fish-like swimming.

First, we employ the form of the *RoboTuna*, a laboratory robot emulating the body shape and motion of a tuna (see Barrett 1996; Barrett *et al.* 1999). We assume the length of the body (from the head to the peduncle, without the caudal fin) to be L . Using curve fitting to describe the shape of the *RoboTuna*, the profile of the body is given as

$$z(x)/L = \pm 0.152 \tanh(6x/L + 1.8) \quad \text{for } -0.3 \leq x/L \leq 0.1, \quad (2.6)$$

$$z(x)/L = \pm(0.075 - 0.076 \tanh(7x/L - 3.15)) \quad \text{for } 0.1 < x/L \leq 0.7. \quad (2.7)$$

At each horizontal position x , the body sections are assumed to be elliptical with a major to minor ratio of $AR = 1.5$, where the major axis corresponds to the height of the body.

The caudal fin has chordwise sections of NACA 0016 shape. The leading edge and trailing edge profiles $x(z)_{LE}$ and $x(z)_{TE}$ are also determined through a curve fitting technique, and are given by

$$x(z)_{LE}/L = 39.543|z/L|^3 - 3.685(z/L)^2 + 0.636|z/L| + 0.7, \quad (2.8)$$

$$x(z)_{TE}/L = -40.74|z/L|^3 + 9.666(z/L)^2 + 0.77, \quad (2.9)$$

where $-0.15 \leq z/L \leq 0.15$.

Thus defined, the geometry of the *RoboTuna* is shown in figure 2(a).

We note that a real tuna body also has other attachments such as dorsal/ventral fins as well as small finlets distributed from the mid-length of the body to the peduncle. With sharp trailing edges, all these secondary fins and finlets are sources of vorticity generation ahead of the caudal fin. The dorsal and ventral fins, on one

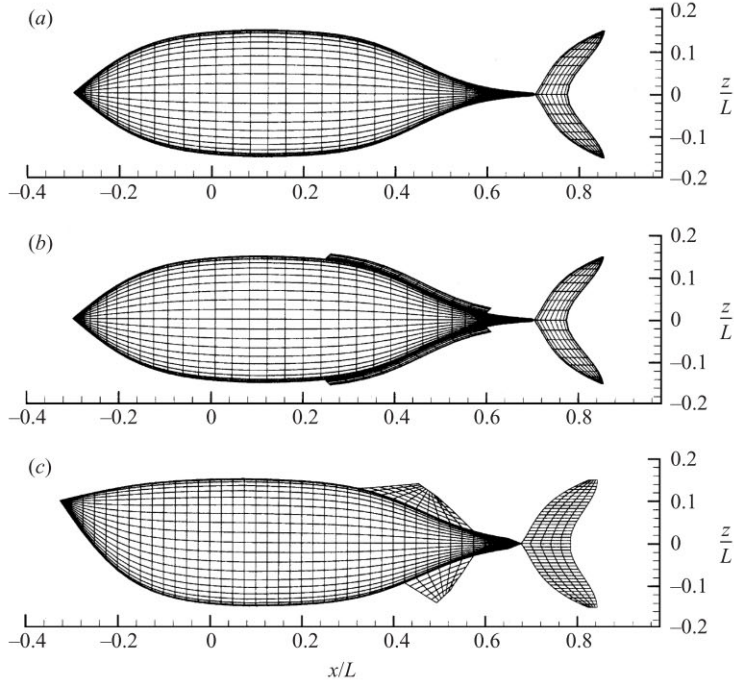


FIGURE 2. Computational geometric forms of (a) the *RoboTuna*, (b) tuna with dorsal/ventral finlets and (c) giant danio.

hand, could only contribute weak vorticity during straight-line swimming since they are located close to the mid-length of the body, where the undulating motion of the body is minimum (cf. § 2.3). The finlets, on the other hand, are expected to shed relatively stronger vorticity due to large lateral motion. For this reason, to study the effect of body-generated vorticity, we add the finlets to the computational tuna body. For simplicity, these finlets are modelled as rectangular strips attached to the contraction region of the dorsal and ventral ridges as displayed in figure 2(b), with cross-sections of NACA 0016 shape and sharp trailing edges on the outer sides.

A third geometry, representing the profile of a giant danio, is adopted (see figure 2c). The body sections are again assumed to be elliptical with a major to minor axis ratio of $AR = 2.2$. If the body length is L , the body shape is measured as (see Anderson 1996)

$$z(x)/L = \pm 0.152 \tanh(6x/L + 1.8) + p(x) \quad \text{for } -0.3 \leq x/L \leq 0.1, \quad (2.10)$$

$$z(x)/L = \pm(0.075 - 0.076 \tanh(6.3x/L - 3.08)) + p(x) \quad \text{for } 0.1 < x/L \leq 0.7, \quad (2.11)$$

where

$$p(x) = 0.0975 \tanh(-(0.3 + x/L)/1.5) + 0.0975. \quad (2.12)$$

The caudal fin has chordwise sections of NACA 0016 shape, to allow efficient resolution of leading-edge suction forces. The caudal fin leading-edge and trailing edge profiles for the semi-span are obtained through a curve fitting technique, and

are given as

$$x(z)_{LE}/L = 39.543|z/L|^3 - 3.685(z/L)^2 + 0.636|z/L| + 0.7, \quad (2.13)$$

$$x(z)_{TE}/L = -40.74|z/L|^3 + 9.666(z/L)^2 - 0.15|z/L| + 0.8075, \quad (2.14)$$

where $-0.15 \leq z/L \leq 0.15$.

In addition, dorsal and ventral fins are added to the body of the giant danio. The fins are attached to the body, along the middle lines of the ventral and dorsal regions, and with cross-sections modelled as NACA 0010 shape. The sharp trailing edges are on the downstream sides. These fins remain attached to the body but are allowed to flex following the prescribed motion of the backbone.

The geometry of the giant danio, complete with the dorsal/ventral fins, is displayed in figure 2(c).

2.3. Kinematics of straight-line swimming

We consider the straight-line swimming of a flexible body with constant speed U in the $-x$ -direction. The relation between the body-fixed coordinate system $oxyz$ and the global coordinate system $OXYZ$ is $x = X + Ut$, $y = Y$ and $z = Z$, where t is the time.

For simplicity, we assume that bending of the fish-like body happens only within the (x, y) -plane, and the tail is assumed to oscillate and rotate as a rigid body while the finlets and secondary fins follow the motion of the body. Hence, our study does not incorporate more complex mechanisms, such as two-plane bending and flexing of the tail, and fin retraction, which may be employed by live fish.

In the straight-line-swimming case, the motion of the body S_b could be fully described by specifying the motion of its backbone with several key kinematic parameters. In this study we choose the same kinematic description as used in the experiments by Barrett (1996), which closely emulates that found in nature (Fierstine & Walters 1968; Dewar & Graham 1994). We assume that the swimming speed U is a constant. The motion is characterized by a travelling backbone wave of smoothly varying amplitude and phase speed c_p which differs from U . The backbone waveform $y(x)$ can be written as

$$y(x, t) = a(x) \sin(k_w x - \omega t), \quad (2.15)$$

$$a(x) = c_1 x + c_2 x^2, \quad (2.16)$$

where $k_w \equiv 2\pi/\lambda$ is the wavenumber, corresponding to wavelength λ , ω is the circular frequency of oscillation, and $x = 0$ is located at a distance 30% of the body length L from the nose, with positive x in the direction from the nose to the tail. The amplitude envelope $a(x)$ is defined with adjustable parameters c_1 and c_2 , achieving a specific value of the double amplitude of motion at the link to the tail.

The front point on the articulated caudal fin where it is attached to the caudal peduncle follows the path of the peduncle, and additionally the fin is allowed to undergo a pitch motion around this front point. This pitch motion has the same frequency ω as the backbone wave-like motion while its temporal phase angle is behind that of the lateral motion of the front point by a phase difference ψ . The tailbeat period $T \equiv 2\pi/\omega$. At any time t , the angle of attack θ with respect to the x -axis is given by

$$\theta = \alpha \sin(k_w x_p - \omega t - \psi), \quad (2.17)$$

where α is the maximum angle of attack and x_p is the x -coordinate of the peduncle.

The frequency scaling of data observed in fish is based on the wake Strouhal law (Triantafyllou, Triantafyllou & Gopalkrishnan 1991; Triantafyllou, Triantafyllou & Grosenbaugh 1993), where the non-dimensional parameter St is written as

$$St = fA/U, \quad (2.18)$$

where $f = \omega/2\pi$ is the tailbeat frequency, A is the mean lateral excursion of the caudal fin at the trailing edge. It was proposed that optimum efficiency is obtained when the large-scale vortical pattern formation is compatible with the dynamics of the wake. More specifically, optimal efficiency behaviour is obtained when the frequency of foil oscillation coincides with the frequency of maximum amplification of vortical disturbances, which is determined from the detailed linear stability analysis of the wake. A discussion of the relation between the disturbances after they have been rolled up into vortices and the produced thrust can be found in Streitlien & Triantafyllou (1998). In defining the Strouhal number, since the width of the wake is not *a priori* known, the lateral excursion of the foil is used. Support from recent fish swimming kinematic data shows that the non-dimensional frequencies are close to the value predicted by wake instability analysis (see e.g. Triantafyllou *et al.* 1993; Rohr *et al.* 1998).

3. Numerical method

To solve the boundary-integral equation (2.2), we apply a panel method. Representations of the time-dependent continuous potential distributions over the body and wake surfaces are developed in discrete form by dividing each surface into quadrilateral panels. The singularity distributions are approximated as centrally collocated piecewise constant over each body and wake panel. Higher panel grid densities are employed in regions of presumed rapid potential variation and in regions with complex geometry, such as tight curvature or lifting surface tips, to increase the accuracy of the unsteady, continuous velocity potential distribution.

3.1. Formulation of the panel method

At any time t , the body perturbation velocity potential at each panel collocation point $\Phi_b(\mathbf{x}_i, t)$ ($i = 1, \dots, N$, where N is the total number of body panels) can be found in terms of the perturbation potentials at all of the other panels, as can be seen by modifying (2.2):

$$-2\pi\Phi_b(\mathbf{x}_i, t) + \sum_{\substack{j=1 \\ j \neq i}}^N \Phi_b(\mathbf{x}_j, t) Q_{ij} = \sum_{j=1}^N \frac{\partial \Phi_b(\mathbf{x}_j, t)}{\partial n} P_{ij}, \quad (3.1)$$

where

$$P_{ij} = \iint_j \frac{1}{r_{ij}} ds, \quad (3.2)$$

$$Q_{ij} = \iint_j \frac{\partial(1/r_{ij})}{\partial n_j} ds, \quad (3.3)$$

$$r_{ij} = |\mathbf{x}_i - \mathbf{x}_j|. \quad (3.4)$$

Application of discrete forms of the Kutta condition and kinematic boundary condition for each panel completes the linear system of equations for $\Phi_b(\mathbf{x}, t)$, the

body perturbation velocity potential over each panel at any given time t , which is expressed from (3.1) in the general form

$$\langle \tilde{Q} \rangle \{ \Phi_b \} = \{ \tilde{P} \}, \quad (3.5)$$

where $\langle \tilde{Q} \rangle$ is the matrix of influence coefficients for the dipole potential distribution; $\{ \Phi_b \}$ is a column vector of the body perturbation velocity potentials; and $\{ \tilde{P} \}$ is the column vector of normal velocity influences for the source potential distribution. Complete details of the linear system development can be found in Wolfgang *et al.* (1999a).

We note that at each time step, the vector \tilde{P} is determined by the motion of the body and the influence from the wake, as expressed by equation (2.1). The body motion is known and the dipole distribution in the wake is predetermined by time history except for the portion at the leading edge.

Coupling the linear system of equations (3.5) with the Kutta condition which determines the strength of the newly shed wake, we solve $\Phi_b(x, t)$ and find the strength of the newly shed dipoles through use of an iterative scheme. The wakes are then updated by moving downstream with the flow field as well as adding new panels at the trailing edges. As a result, the total number of wake panels N_w increases with time, while the number of body panels remains constant. The wakes are convected as material surfaces by the fluid velocity field, deforming under the influence of the body motions and of the self-induced velocities found from a desingularized Biot-Savart law. The numerical scheme is integrated over time using a first-order forward-difference algorithm.

To find the induced velocity field, a body and wake panel desingularization technique is employed (Krasny 1986) which removes the singularities from the discrete potential distributions. Each wake and body panel therefore is assigned a core radius, δ_b and δ_w , respectively; thus, the desingularized velocity field induced by a vortex ring making up the sides of a wake panel which is equivalent to the distributed dipoles within the element, for instance, can be written as a desingularized Biot-Savart law:

$$V(x) = \frac{\Gamma}{4\pi} \oint \frac{s \times r}{r^3 + \delta_w^3} dl, \quad (3.6)$$

where Γ is the circulation of the vortex ring, s is the tangent vector to the panel, r is the vector with magnitude r from the element to the field point, and the path of integration is along the sides of the panel. As x approaches the vortex ring, r approaches zero, and the velocity field expressed by (3.6) approaches a finite limit.

By imitating the effect of viscosity in a real fluid through the generation of finite-thickness shear layers, the desingularization technique eliminates the associated ill-posedness of the dynamic evolution of the shear layers. The inclusion of the desingularization is a necessity in the prevention of nonlinear energy transfer to the highest wavenumber modes and of simulation breakdown or non-physical solution growth caused by numerical instabilities resulting from the ill-posed problem. Additionally, when upstream-shed vorticity impinges on downstream body elements, non-physical free-wake acceleration and deformation is avoided through desingularization of the body surface panels. Without this body desingularization, free-wake panels interacting with flexing body panels may convect inside the body. A detailed description of the implementation of the present panel solver is found in Katz & Plotkin (1991).

$N_b \setminus N_c$	50	100	200	400
25	2.09	2.34	2.28	2.26
100	1.15	1.37	1.32	1.29
400	1.12	1.33	1.28	1.26
1600	1.11	1.33	1.28	1.26

TABLE 1. Convergence of the mean thrust force $F = -F_x$ (in N) on a straight-line-swimming tuna with respect to the number of panels on the body N_b and the number of panels on the caudal fin N_c . The time step $\Delta t = T/32$.

$T/\Delta t$	8	16	32	64
	1.44	1.23	1.26	1.27

TABLE 2. Convergence of the mean thrust force $F = -F_x$ (in N) on a straight-line-swimming tuna with respect to the time step Δt . $N_b = 1600, N_c = 400$.

3.2. Validations

The unsteady three-dimensional code was validated through a series of systematic tests, employing a variety of numerical parameters to evaluate the integrated dynamics against documented experimental results and against self-performance as the parameters were changed to approach the continuous solution.

3.2.1. Convergence tests

We apply the *RoboTuna* geometry with body shape shown in figure 2(a) as the test case. To match the size of the *RoboTuna* applied in experimental studies (Barrett 1996), the length L is set to be 1.066 m.

We choose swimming velocity $U = 0.7 \text{ m s}^{-1}$, body wavelength $\lambda \equiv 2\pi/k_w = 1.047 \text{ m}$, Strouhal number $S_t = 0.183$, and kinematic parameters $c_1 = 0.00294$ and $c_2 = -0.111 \text{ m}^{-1}$. Convergence of the present numerical method was confirmed by varying the time step size Δt and the number of panels over the body surface. The value of the mean thrust force \bar{F} is chosen to demonstrate the performance of the numerical solver.

We first check the convergence of the computation with respect to N_b , the number of panels employed on the surface of the body excluding the tail, and N_c , the number of panels on the caudal fin. As shown in table 1, the mean thrust force on the fish converges linearly with respect to both N_b and N_c , which confirms the performance expectation of the panel method.

For the time evolution, we apply a first-order forward-difference method with an accuracy of $O(\Delta t)$, where $O(\Delta t)$ is the time step. From table 2, we see that the mean thrust force converges as we reduce the time step. Other numerical parameters that may influence the accuracy of the results are the desingularization factors employed to eliminate the singularities (cf. § 3.1). As we can see from table 3, the variation of results is small over a large range of the body desingularization factor δ_b and the wake desingularization factor δ_w . In the following study, δ_b and δ_w are chosen to be within this range.

Based on these convergence tests, in the following computations we choose $N_b = 1600$, $N_c = 400$ and $\Delta t = T/32$. With those parameters the expected numerical error is less than 1%. In the cases with attached finlets or secondary fins, denser

$\delta_b/L \setminus \delta_w/L$	0.005	0.01	0.05	0.5
0.005	1.26	1.29	1.29	1.28
0.01	1.31	1.26	1.26	1.26
0.05	1.31	1.27	1.26	1.25
0.5	1.31	1.27	1.26	1.26

TABLE 3. Sensitivity of the mean thrust force $F = -F_x$ (in N) on a straight-line-swimming tuna with respect to the body desingularization factor δ_b and the wake desingularization factor δ_w . Time step $\Delta t = T/32$, $N_b = 1600$, $N_c = 400$.

computational grids with 200 computing panels on each of these parts are employed to ensure accuracy.

3.2.2. Comparison with experimental data

We compare the numerical results obtained for the power input for a swimming *RoboTuna* (Body A) with those obtained experimentally by Barrett *et al.* (1999). Due to the fact that in the experiment it is impossible to separate thrust from drag, the only quantity left for comparison is the power input P . As shown in table 4, the power input obtained through numerical simulations differs from the experimental results with a discrepancy ranging from about 1% to 20%. In general, cases with larger oscillation frequencies and maximum angles of attack tend to show larger errors. Not considering errors in experimental measurements, this discrepancy could be caused by the following factors. First, the numerical scheme is based on the assumption that the flow is inviscid except for a thin wake shed by the tail or rear part of the fish. The separation line is fixed and no skin friction or turbulence effects are accounted for. Second, we note that there are some differences between kinematics in the experimental and numerical cases. In the experiments, the robotic fish is separated into five rigid sections and each one of them undergoes prescribed angular motions to achieve the wave-like motion (see Barrett *et al.* 1999). In the numerical simulations, on the other hand, the backbone motion is set to be a continuous function from head to the peduncle. Finally, the numerical model does not take into account the effect of leading-edge separation from the caudal fin, which may play an important role when the angle of attack is large.

4. Three-dimensional flow structure around a swimming fish

In this section we examine the near-body flow for the straight-line-swimming motions of a tuna and a giant danio, employing computational bodies shown in figures 2(b) and 2(c).

A fish body has moderate length to width ratio. As a result, the flow patterns are expected to be a mixture of two extreme cases: the two-dimensional body flow described by Wu (1961) for an infinite span to length ratio, and the slender body flow described by Lighthill (1970) for small span to length ratio. Figure 3 illustrates the near-body flow pattern resulting from the two-dimensional swimming theory of Wu (1961), versus the three-dimensional, slender-body theory of Lighthill (1970). In figure 3(a), the actuated flow travels along streamlines laterally away from the fish and parallel to the direction of swimming; hereafter this flow pattern is referred to as ‘longitudinal’. The flow patterns shown in figure 3(b), hereafter referred to as

	Case 1	Case 2	Case 3	Case 4	Case 5	Case 6
Strouhal number St	0.133	0.183	0.201	0.196	0.281	0.413
Swimming speed (m s^{-1})	0.7	0.7	0.7	0.7	0.7	0.7
Wavelength λ (m)	1.475	1.047	1.047	1.227	1.207	1.675
Oscillation frequency ω (rad s^{-1})	3.306	6.858	7.295	5.052	8.390	13.0
Maximum angle of attack α (deg.)	0.97	8.35	11.54	11.81	17.77	18.76
Tail phase ϕ (deg.)	80.0	80.0	97.7	97.7	97.7	85.0
Amplitude coefficient c_1	0.00236	0.00294	0.00294	0.0040	0.00042	0.00236
Amplitude coefficient c_2 (m^{-1})	-0.163	-0.111	-0.098	-0.146	-0.108	-0.114
Tail excursion A (m)	0.177	0.117	0.120	0.171	0.147	0.140
Mean thrust force (computation) (N)	0.93	1.26	1.20	1.35	2.24	4.92
Mean power input (experiment) (W)	1.01	1.13	1.12	1.34	2.04	5.68
Mean power input (computation) (W)	1.02	1.23	1.28	1.35	2.45	5.50
Mean power input error (%)	0.99	8.8	14.3	0.75	20.1	3.2
Computed propulsive efficiency η (%)	63.5	71.7	65.7	69.6	64.2	62.6

TABLE 4. Summary of kinematic and performance data for the *RoboTuna*. Comparison between experimental measurements on the *RoboTuna* robotic instrument and the numerical simulation results for five cases are shown. Body type (a) (figure 2) is employed for simulations, with caudal fin wake shedding only. The length of the body (excluding the caudal fin) $L = 1.066$ m.

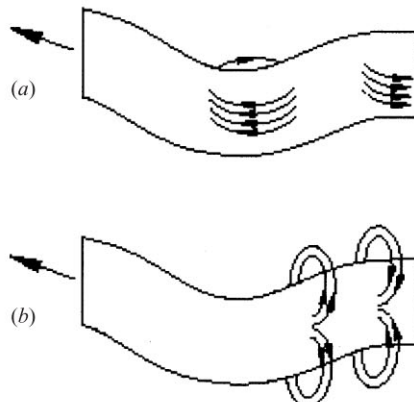


FIGURE 3. Depiction of near-body velocities in straight-line swimming as modelled by the classical swimming theories of (a) Wu (1961), two-dimensional swimming plate theory and (b) Lighthill (1975), three-dimensional slender-body theory.

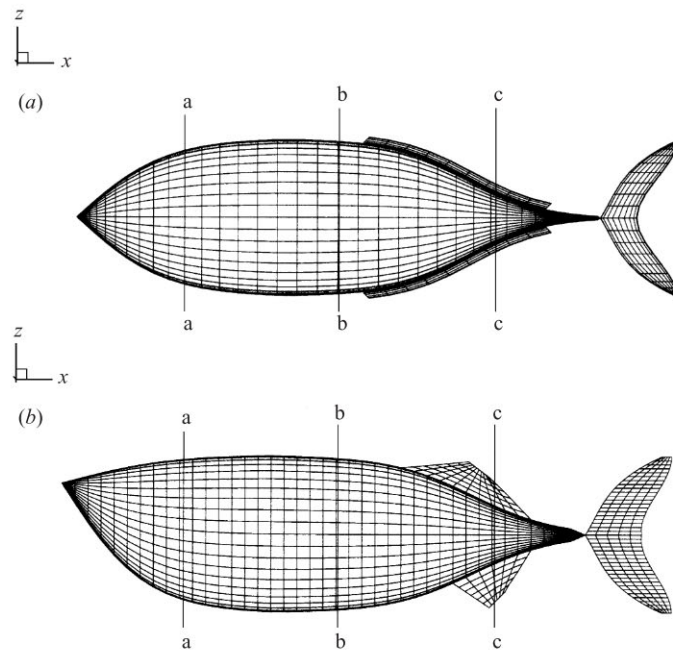


FIGURE 4. Location of sectional cuts along the length of (a) the tuna and (b) the giant danio computational geometry during straight-line swimming.

'transverse', show the fluid to travel laterally away from and sectionally around the depth extremes of the geometry.

We apply the panel method to study the near-body flow pattern during the straight-line swimming of a fish: we show the velocity field which is obtained directly from the simulation, and the vorticity field which is evaluated by calculating the curl of the velocity field with a central-difference algorithm. We display these two fields in the horizontal mid-depth plane of the fish body, as well as three sectional cuts parallel to the (y, z) -plane at different locations along the length of the body, tagged as cuts a-a, b-b and c-c as shown in figure 4. The first section, cut a-a, is located near

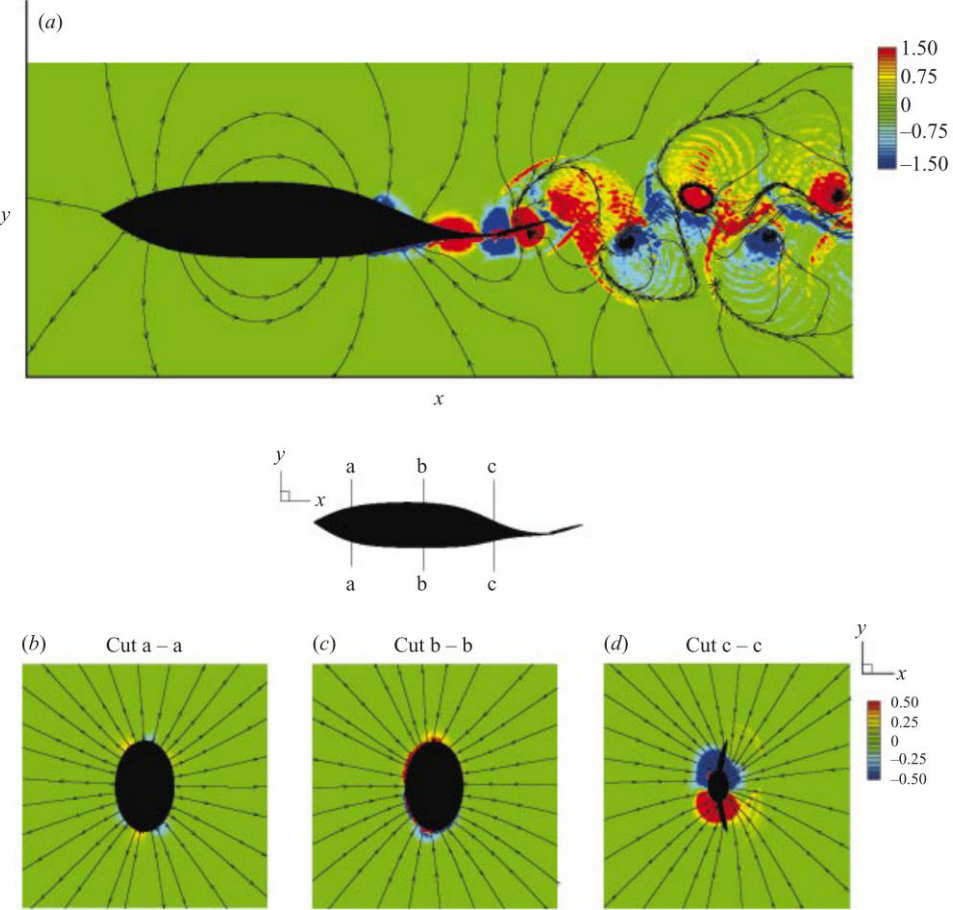


FIGURE 5. Sectional flows at $t = 3T$ during the straight-line swimming of the tuna (body b). We show: (a) a top view of the streamlines of the planar cut of the flow at the mid-depth level of the fish body, superimposed on colour contours of the vertical component ω_z of the vorticity; and inplane streamlines on colour plots of the longitudinal vorticity ω_x in sections (b) a–a, (c) b–b and (d) c–c. Section views are taken looking from tail towards the head and all the vorticity components are normalized by U/L . All the kinematic parameters are for case 6 in table 4 (note that this is the same as the constructive interference case discussed later on).

the head where the sectional area of the body is increasing. The second section, cut b–b, is located at the fish mid-body, where the sectional area is constant. Cut c–c is positioned in the contraction region near the caudal peduncle and, in the case of the giant danio, at the trailing edge of the dorsal fin.

Figure 5 illustrates the near-body flow at the three sectional cuts at time $t = 3T$ with kinematic parameters specified by case 6 in table 4. In-plane streamlines are superimposed on the colour plots of the strength of the longitudinal vorticity ω_x . In addition, a top view of the flow within the mid-depth plane is provided for visual correlation with the sectional views, having the in-plane streamlines superimposed on the plot showing the strength of the vertical components of vorticity ω_z . Note that in the potential flow model employed in the current investigation, the vorticity is supposed to be zero except on the wake sheets. However, due to the application of

desingularization (cf. § 3.1), which to some extent replicates the effect of viscosity, a finite amount of vorticity is spread into the fluid.

In the top view of the mid-depth plane flow, the reverse Kármán vortex street is clearly seen, together with an induced jet flow between the vortex pairs (see e.g. Kármán & Burgess 1935). The sectional flows shown in figure 5(b–d) all display a dominant longitudinal pattern. Only in the rear region of the body does some longitudinal vorticity in the x -direction appear, near the top and bottom of the fish body. This x -vorticity generated by the finlets induces a certain amount of transverse flow, which is, however, quite weak compared with the longitudinal flow. Overall, the longitudinal patterns dominate over much of the body depth. Snapshots of the flow field for other time instants during a swimming cycle are qualitatively similar to those shown in figure 5. Systematic studies with other kinematic parameters given in table 4 also demonstrate the same flow pattern.

We now study the case of the giant danio. Following the experimental measurements by Anderson (1996), the body length L for the danio is 0.073 m. The kinematic parameters which prescribe the motion are also measured from experimental DPIV images (see Anderson 1996), specifically: swimming speed $U = 0.08 \text{ m s}^{-1}$; tailbeat frequency $f = 3.3 \text{ Hz}$; backbone wavelength $\lambda = 0.08 \text{ m}$; Strouhal number $S_t = 0.50$; backbone wave parameters $c_1 = 0.004$ and $c_2 = -2.33 \text{ m}^{-1}$; phase angle between the pitch of the tail and heave of the peduncle $\phi = 96^\circ$; and maximum tail angle of attack $\alpha = 6^\circ$.

In figure 6, the top view of the flow within the mid-depth plane is similar to that in figure 5, with a reverse Kármán vortex street being formed in the wake. At cut a–a, where the transverse motion of the body is small, near-body flow dynamics at the head reveal a longitudinal-type actuation, as fluid is displaced laterally over the entire depth. At cut b–b, near-body flow dynamics at the mid-section reveal combined longitudinal and transverse actuation patterns, as fluid is directed laterally away and sectionally around the body. Near-body flow dynamics around cut c–c in the contraction region also reveal a complex longitudinal/transverse actuation pattern with a stronger transverse flow, while the bound vorticity strength grows along the length of the fish. The three-dimensionality of the flow is strongest near the upper and lower edges of the fish, where a large longitudinal vorticity ω_x exists. Similar flow patterns are observed for other times t as well.

The cause of the difference in flow structures for the tuna and giant danio lies in the difference in swimming kinematics. Considering the sectional flow within transverse cuts along the body length parallel to the (y, z) -plane, qualitatively it contains a flow pattern symmetric with respect to z , representing the steady flow around the stretched straight body, and an asymmetric pattern caused by the lateral motion resembling the two-dimensional flow around a cylinder. The magnitudes of these two patterns are determined by the steady speed, the lateral speed and the body geometry. For the tuna the ratio of the maximum transverse speed and the forward speed is lower than 1.1 for all the combinations of swimming parameters listed in table 4, resulting in a longitudinal flow for much of the body length. For the giant danio, however, this ratio rises to 1.5 close to the tail, leading to stronger transverse flow around the contraction part of the danio body as we observed in our numerical simulations.

To summarize, in the case of the tuna, the flow is mostly longitudinal, while for the giant danio, the flow around the fish can be shown to be neither entirely longitudinal nor transverse. Rather, combinations of longitudinal and transverse features are prevalent along the length of the fish body. For this reason, it can be seen

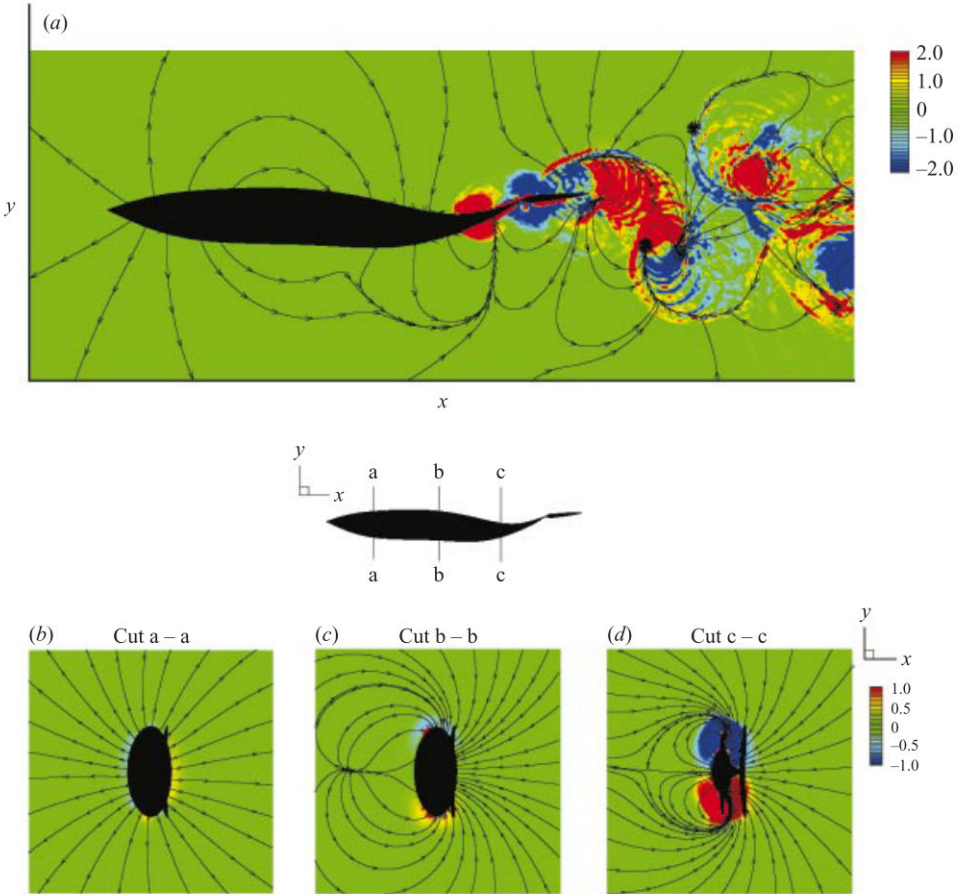


FIGURE 6. Sectional flows at $t = 3T$ during the straight-line swimming of the giant danio. We show: (a) a top view of the streamlines of the planar fluid superimposed on colour contours of the vertical component ω_z of the vorticity at the mid-depth plane; and inplane streamlines with longitudinal vorticity ω_x in sections (a) a–a, (b) b–b and (c) c–c. Section views are looking from tail to head and all the vorticity components are normalized by U/L .

that simplified models of near-body flow dynamics may underestimate performance measures such as efficiency and overestimate the thrust and power required for swimming, and hence the drag on an undulating body (see e.g. Wu 1971c; Newman 1973; Newman & Wu 1973; Lighthill 1975). This description is in agreement with the quantitative findings of vortex lattice theory (Cheng *et al.* 1991), which has been used to predict the swimming performance of low-aspect-ratio swimming plates whose performance is somewhere between the estimates of the two-dimensional theory and slender body theory.

5. Vorticity control mechanisms

In this section we investigate the principal vorticity control mechanisms that may be utilized by a swimming fish by studying the interaction of wakes shed from the caudal fin and the body.

Vorticity control is the process of altering the position and strength of oncoming vortices, and the generation of additional vorticity, thereby affecting the load distri-

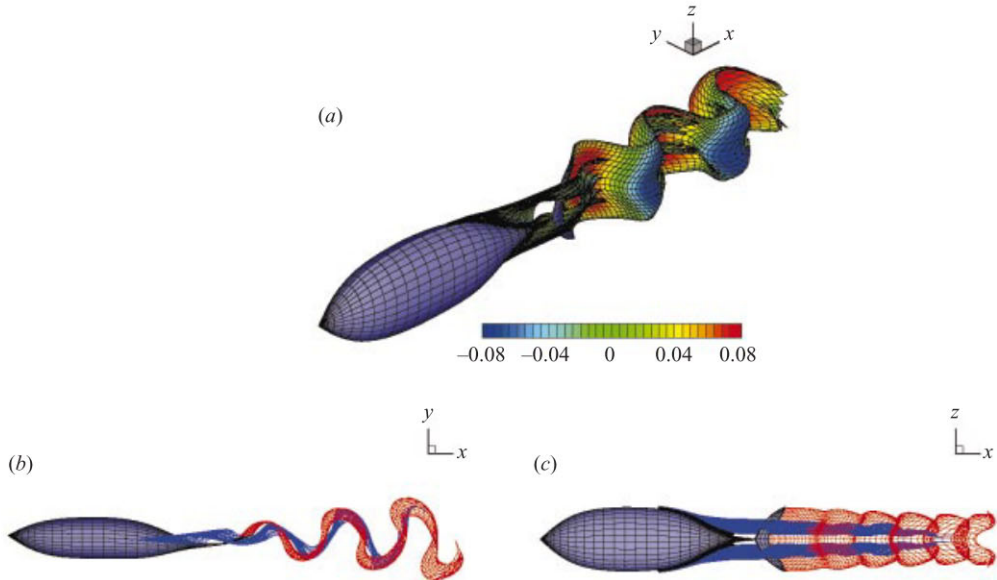


FIGURE 7. (a) Formation of the wake sheets of a straight-swimming tuna (body *b*) at $t = 3T$, contoured by the distribution of dipole strength (normalized by UL), and (b) the top and (c) side views of the position of the wake sheets shed from the tail (red) and the dorsal/ventral fins (blue). All the kinematic parameters are for case 6 in table 4.

bution on the body and the unsteady fluid dynamics. The control of vorticity can be accomplished through the unsteady motion of a body in a fluid or the unsteady forcing of the flow (see e.g. Ffowcs Williams & Zhao 1989; Tokomaru & Dimotakis 1991; Triantafyllou *et al.* 2000). Unsteady foil propulsion offers high efficiency and the capability for high thrust production. Gursul & Ho (1992) demonstrated that unsteady motion of airfoils can cause a very high lift coefficient, and work by Anderson *et al.* (1998) shows that oscillating foils are able to produce propulsive thrust very efficiently. Experimental and computational works on the performance of an oscillating lifting surface in the presence of oncoming vorticity (Koochesfahani & Dimotakis 1988; Gopalkrishnan *et al.* 1994; Anderson 1996; Streitlien, Triantafyllou & Triantafyllou 1996) reveal that proper phasing between the foil motion and the encounter with oncoming vorticity can yield a significant increase or decrease in efficiency. The principal modes of foil–vortex interaction with a street of alternating-sign vortices can be summarized as (Gopalkrishnan *et al.* 1994):

(a) *Vorticity annihilation*, where foil-generated vorticity interacts destructively with the oncoming vorticity, resulting in the generation of a weak vortex street downstream of the foil. Repositioning of the oncoming vorticity may result in a drag-type street or a jet-type stream. In the latter case, the efficiency of propulsion is maximized.

(b) *Constructive interference*, where foil-generated vorticity interacts constructively with the oncoming vorticity, resulting in the generation of a strong vortex street downstream of the foil. Repositioning of the oncoming vorticity may result in a drag-type street or a jet-type stream; in either case, the drag or thrust force production is maximized.

(c) *Vortex pairing*, where foil-generated vorticity interacts with an oncoming vortex of the opposite sign, resulting in the generation of pairs of vortices (four vortices per cycle). The interaction may result in a drag-type wake, or a jet-type wake. Depending

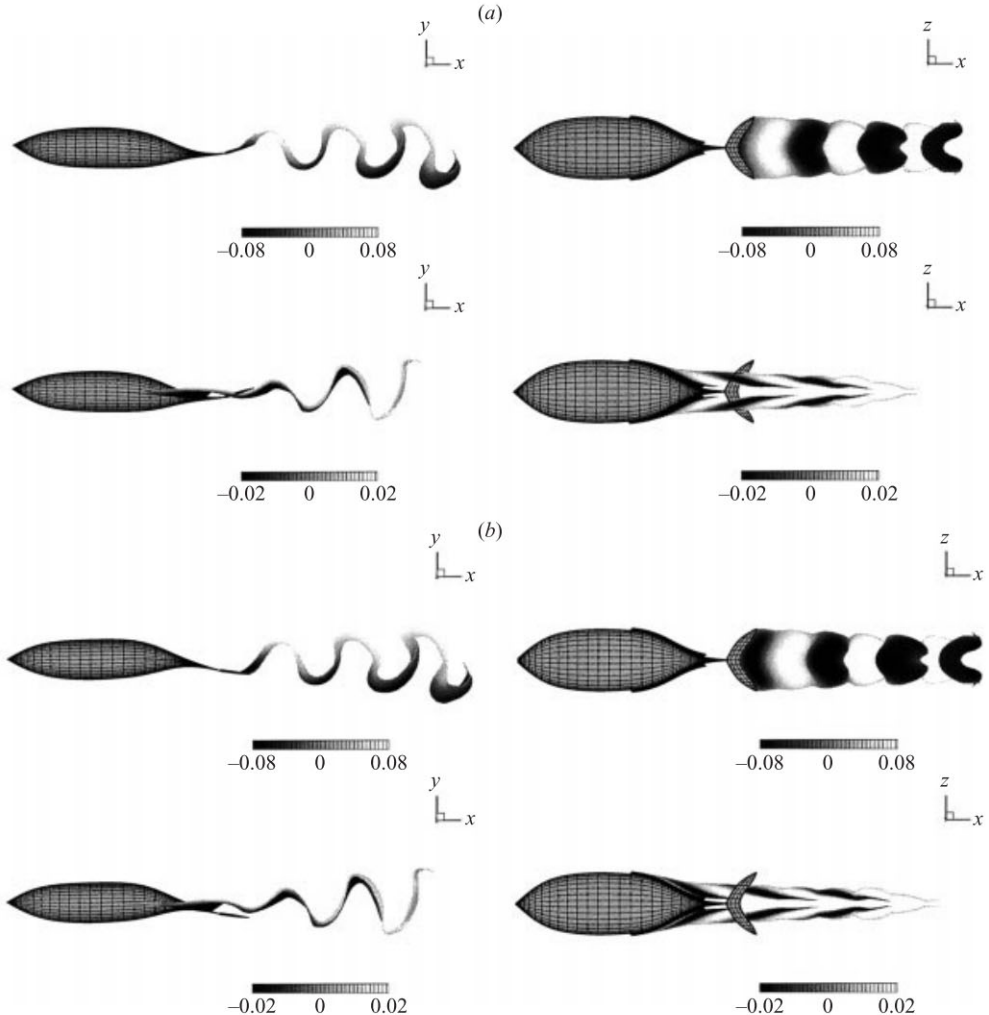


FIGURE 8(a, b). For caption see facing page.

on the pairing process, the efficiency can be close to the annihilation mode maximum, or to the constructive interference minimum, or somewhere in between. For inviscid schemes, such as used in Streitlien *et al.* (1996) and the present approach, vorticity annihilation is not a possibility. Instead, vortex pairing with very small distance between the centres of opposite-sign vortices replaces the annihilation mode; and is associated with the maximum achievable efficiency.

5.1. Vorticity control by the tuna

We investigate the vorticity control utilized in the straight-line swimming of a tuna (body type *b* in figure 2) with body-bound vortices shed from the dorsal and ventral finlets. To illustrate the interaction between the vortices generated by the tail and the finlets, we study the relative position and phase relation between the dipole sheets shed from the trailing edges of these lift surfaces, as shown in figure 7. The strength of the dipole distribution on these sheets is defined to be positive if the dipoles point to the right-hand side of the sheet. The numerical results show that the tail-generated

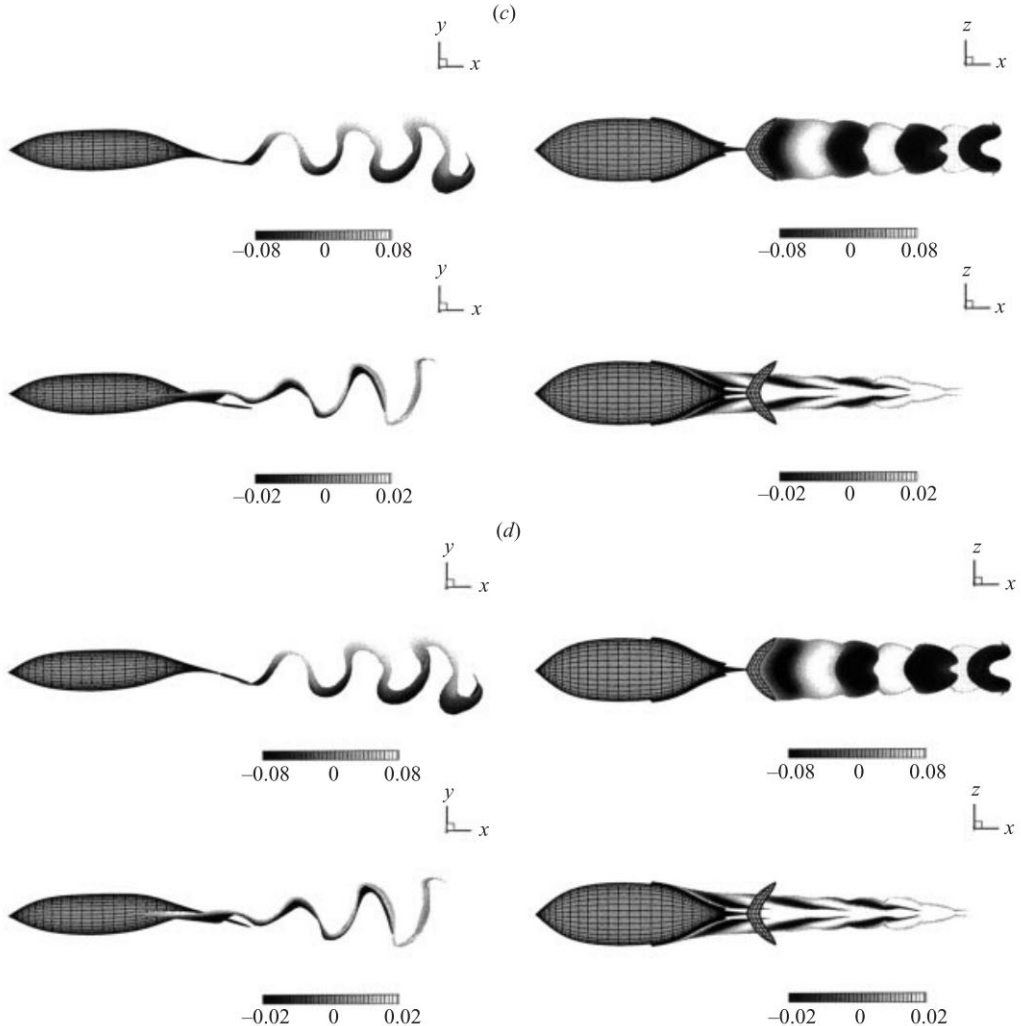


FIGURE 8. Top and side view of the wake formation of a straight-swimming tuna in the constructive interference case over half a tailbeat period starting from $T_0 = 3T$: (a) $t = T_0$, (b) $t = T_0 + T/8$, (c) $t = T_0 + T/4$, (d) $t = T_0 + 3T/8$. At each instant, the top figures show the distribution of dipole strength on the tail-shed wake while the lower figures show the distribution of dipole strength on the fin-shed wake. The dipole strength is normalized by UL . All the kinematic parameters are for case 6 in table 4.

dipole sheet is several times stronger than those shed from the finlets; therefore, the wake is dominated by vorticity created by the tail.

5.1.1. Constructive interaction

The phase of encounter between the oscillating caudal fin and the body-generated vorticity, released upstream through sharp finlets or secondary fins, significantly affects subsequent wake–wake interaction dynamics. This phase of encounter is dependent on the wavelength of the backbone wave λ , the longitudinal distance between the trailing edges of the dorsal/ventral fins and the leading edge of the caudal fin, and the phase speed of the backbone wave with respect to the swimming speed c_p/U .

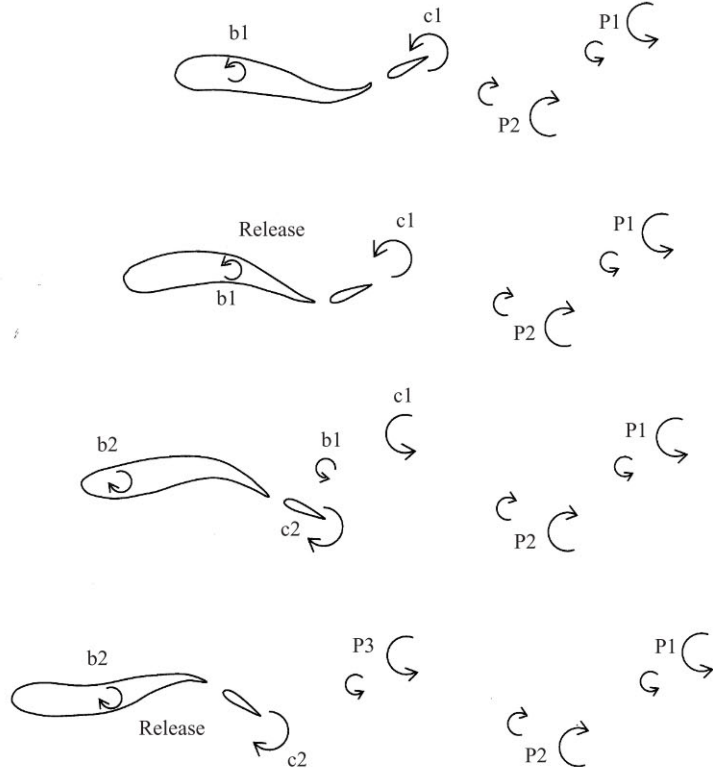


FIGURE 9. Vorticity control mode 1 – *constructive interference*. The four sketches in this series shown top to bottom correspond to the four instants in figure 8. They illustrate the manner in which vortices shed from upstream separation lines are manipulated by the oscillation of the articulated caudal fin to amplify the strength of the wake in a constructive interference pattern.

As can be seen from figure 8, the tail- and finlet-generated vortex sheets are apart when they reach the caudal fin. As they travel downstream, however, the three sheets are drawn together by each other's induced velocity field until they almost overlap in space. The same phenomenon is observed in all the wake–wake interfering cases shown in this paper. This repositioning process is understandable since away from the body the evolution of the tail- and body-bound wake sheets is determined by the same flow field and any points on these sheets close to each other would travel together.

Figure 8 displays the distribution of dipole strength in both the tail wake and the fin wake over half a tailbeat period. The kinematic parameters are the same as those employed in figure 5. By comparing the plots in figure 8 at $t = T_0$ with the vorticity field in figure 5(a) which is at the same moment, we find that a concentration of positive dipoles (dipoles pointing to the right-hand side of the sheet), shown as a light area in the wake sheets, corresponds to a counterclockwise vortex (looking from above). A concentration of negative dipoles (dark area in the wake sheets), on the other hand, represents a clockwise vortex. Reverse Kármán vortex streets are created by the wakes of the caudal fin and the dorsal/ventral finlets. The vortices in the tail wake and the body wakes travel close to each other while they have the same rotational sign, as displayed in figure 9, a sequence of sketches roughly corresponding to the snapshots at four instants in figure 8. In this constructive interaction mode, the

	Mean thrust (N)	Oscillation of thrust (N)	Mean power input (W)	Oscillation of power input (W)	Efficiency η (%)
Case 6					
Body (a)	4.92	6.52	5.50	6.39	62.6
Body (b)	5.70	6.67	6.32	6.45	63.1
Case 2					
Body (a)	1.26	1.58	1.23	1.39	71.7
Body (b)	1.29	1.44	1.21	1.31	74.6

TABLE 5. Mean value and amplitude of oscillation of the thrust force and power input for the straight-line swimming of a tuna with (body b) or without (body a) dorsal/ventral finlets. All the kinematic parameters are for cases 6 and 2 in table 4.

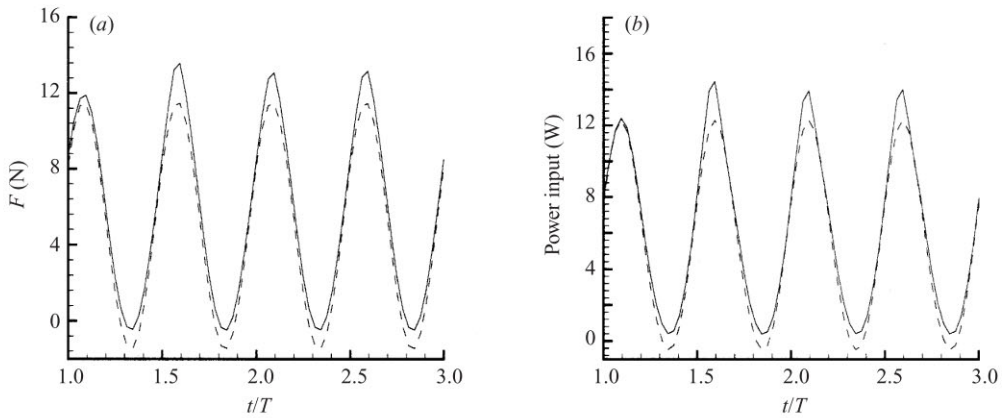


FIGURE 10. Time history of (a) the thrust $F = -F_x$ and (b) power input for a straight-line-swimming tuna with (—) or without (---) dorsal/ventral finlets in the constructive interaction case. All the kinematic parameters are for case 6 in table 4.

body- and tail-generated wakes strengthen each other, resulting in a stronger overall jet wake.

Figure 10 shows the time history of the thrust and power input, compared with the case without vorticity shedding from the body (body type *a* in figure 2). We see that in the constructive interference mode, both the peak value and the amplitude of oscillation of the thrust force are increased. When steady state (limit cycle) is reached after about 2 tailbeat periods, we perform Fourier analysis to obtain the mean and amplitude of oscillation of the thrust and power input, as displayed in table 5. Due to the vorticity shedding from the body and its constructive interaction with the tail-generated wake, these quantities are all increased compared to those in the case without body vortex shedding. Meanwhile, the propulsive efficiency η , defined as the ratio between the mean thrust times the speed and the mean power input, remains virtually unchanged.

5.1.2. Destructive pairing of body- and tail-generated wakes

To explore other possible vorticity control modes, we examine the problem with parameters specified by case 2 in table 4. Figure 11 shows the tail- and body-generated wake sheets over half a tailbeat period. Again, both wakes are repositioned towards

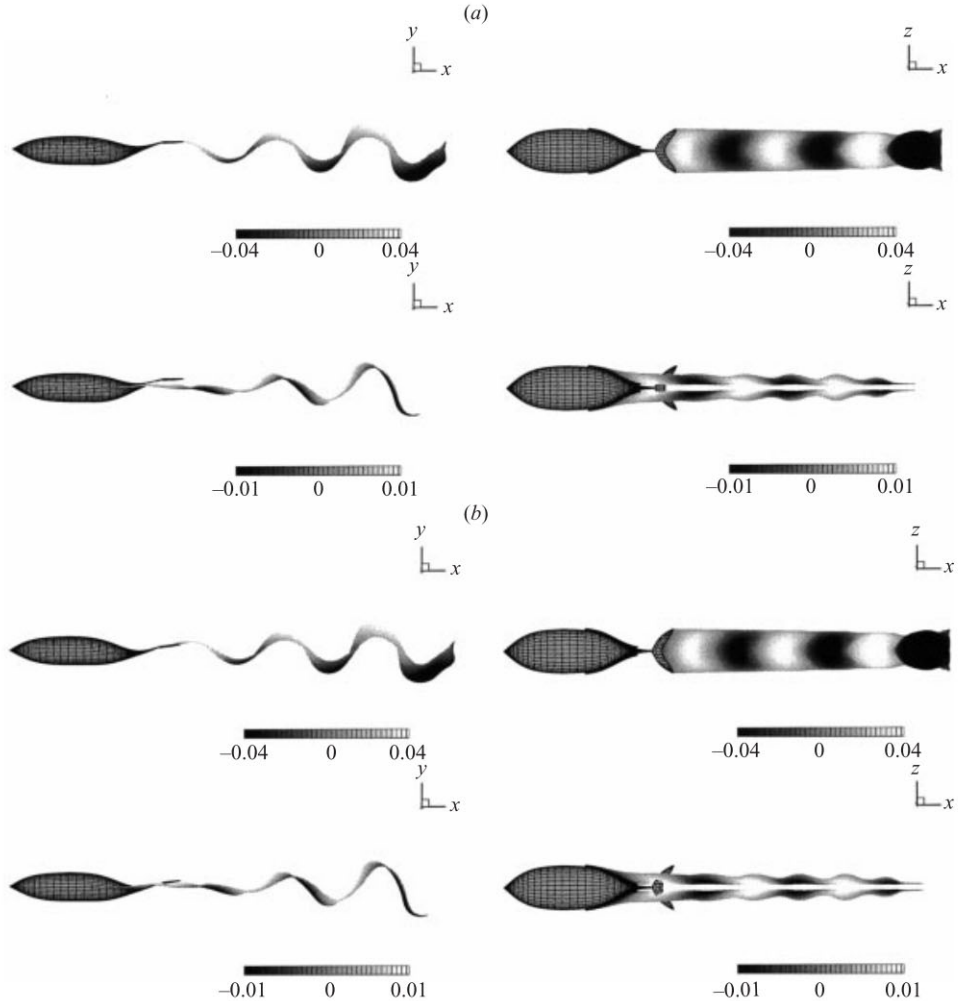


FIGURE 11(a,b). For caption see facing page.

each other in the downstream region. Unlike the previous case, however, the vortices that come close to each other have opposite rotational sign, as in the sketches in figure 12. Since the two vortices close to each other cannot merge into one within the present potential flow model, vortex pairs are formed and lead to the destructive pairing mode mentioned above.

The thrust and power input of this destructive pairing-off case are displayed in figure 13, with the mean value and amplitude of oscillation shown in table 5. It is seen that although both the peak value and the amplitude of oscillation of the thrust are reduced by the destructive wake interactions, the mean thrust is actually increased a little. The most conspicuous feature of this mode is the increase of the propulsive efficiency, as in the destructive vortex interaction case studied by Gopalkrishnan *et al.* (1994). The increase in swimming efficiency suggests that the fish may recover some of the energy lost to wake generation upstream and generate thrust more efficiently.

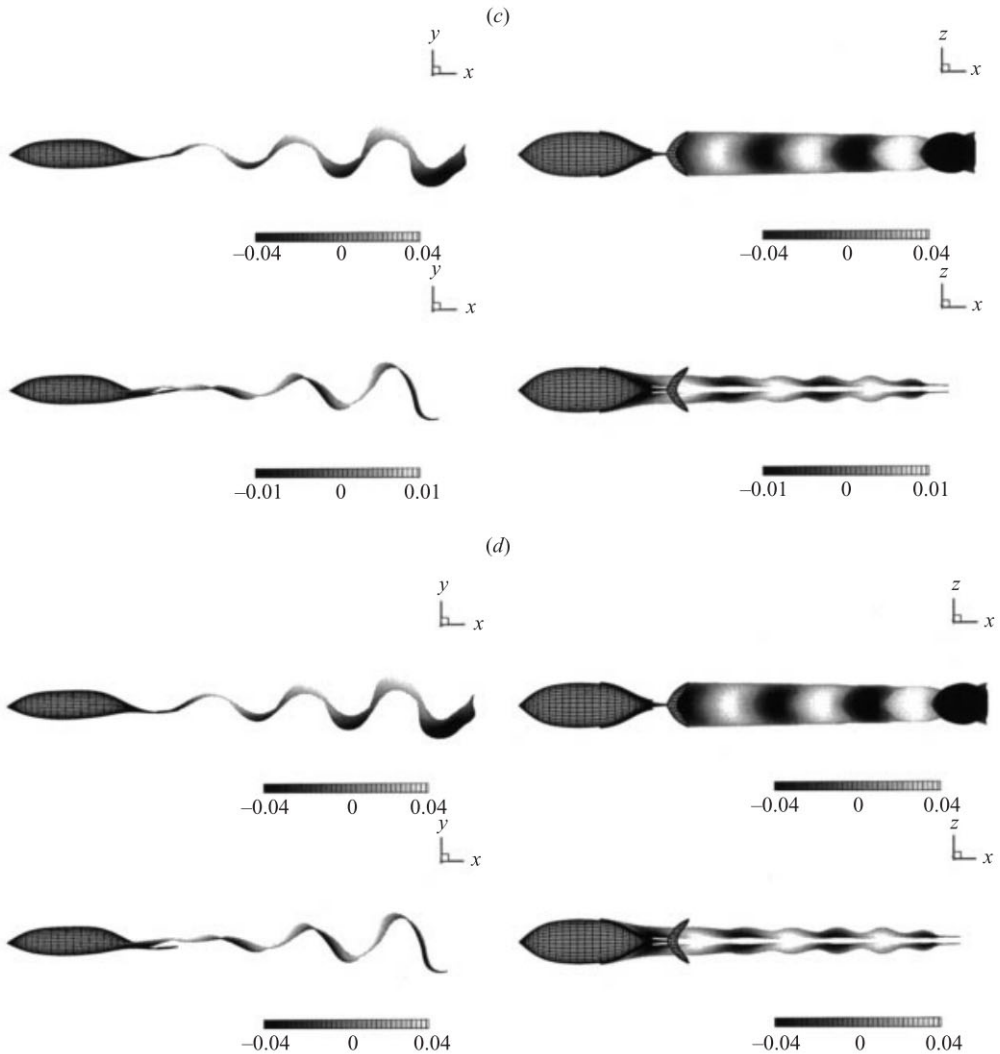


FIGURE 11. Top and side view of the wake formation of a straight-swimming tuna in the destructive interference case over half a tailbeat period starting from $T_0 = 3T$: (a) $t = T_0$, (b) $t = T_0 + T/8$, (c) $t = T_0 + T/4$, (d) $t = T_0 + 3T/8$. At each instant, the top figures show the distribution of dipole strength on the tail-shed wake while the lower figures show the distribution of dipole strength on the fin-shed wake. The dipole strength is normalized by UL . All the kinematic parameters are for case 2 in table 4.

5.2. Vorticity control by the giant danio

Using the experimentally observed kinematic parameters for the swimming of a giant danio, the interference mode between the vortices shed from the caudal fin and those from the attached dorsal and ventral fins is identified as the destructive pairing-off case, as shown in figure 14. Due to the fact that the wake sheets have a larger lateral excursion than in the tuna cases, certain wake features are seen more clearly here. For instance, in figure 14 one notable phenomenon is the switching of the body-generated wakes from a reverse Kármán street configuration as they are shed from the fins, to a Kármán vortex street arrangement as they go downstream due to the repositioning

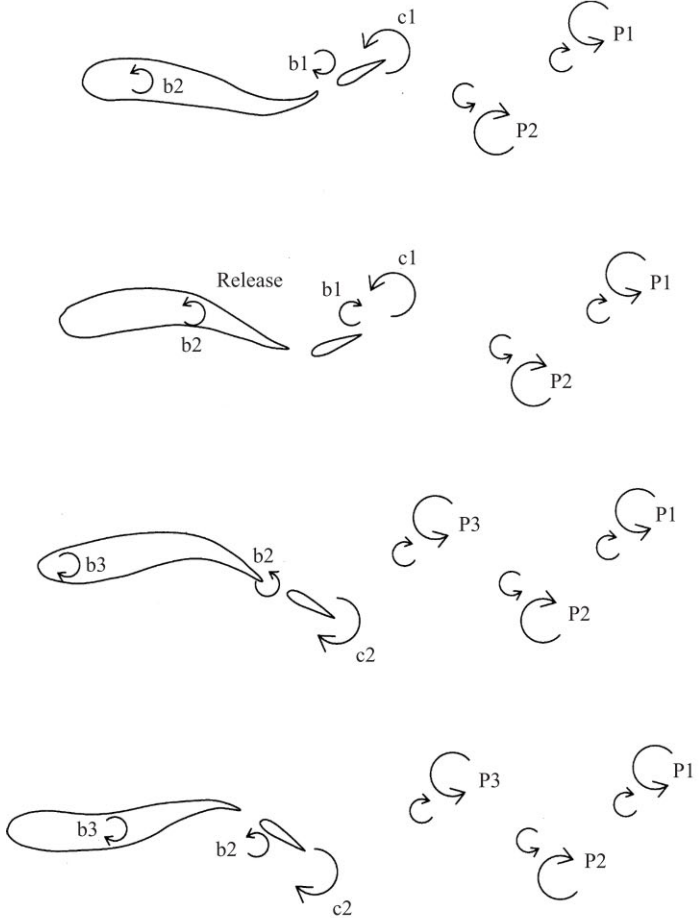


FIGURE 12. Vorticity control mode 2 – *destructive interference*. The four sketches in this series shown top to bottom correspond to the four instants in figure 11. They illustrate the manner in which vortices shed from upstream separation lines are manipulated by the oscillation of the articulated caudal fin to decrease the strength of the total wake produced.

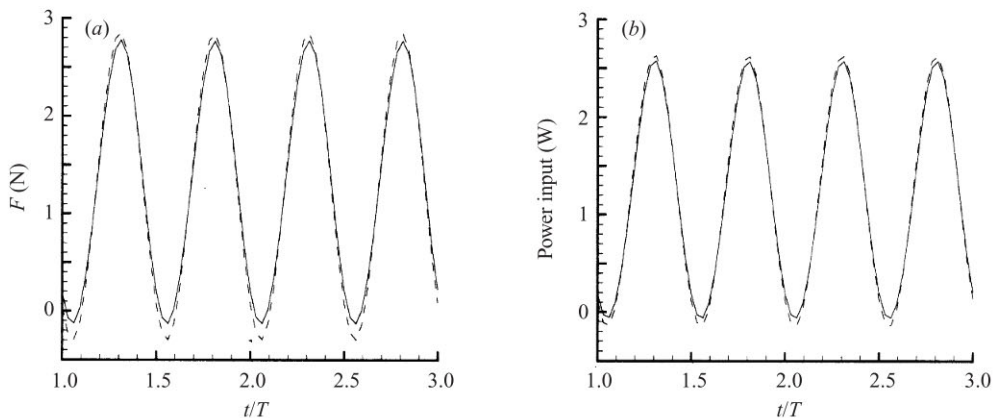


FIGURE 13. Time history of (a) the thrust $F = -F_x$ and (b) power input for a straight-line-swimming tuna with (—) or without (---) dorsal/ventral finlets in the destructive interaction case. All the kinematic parameters are for case 2 in table 4.

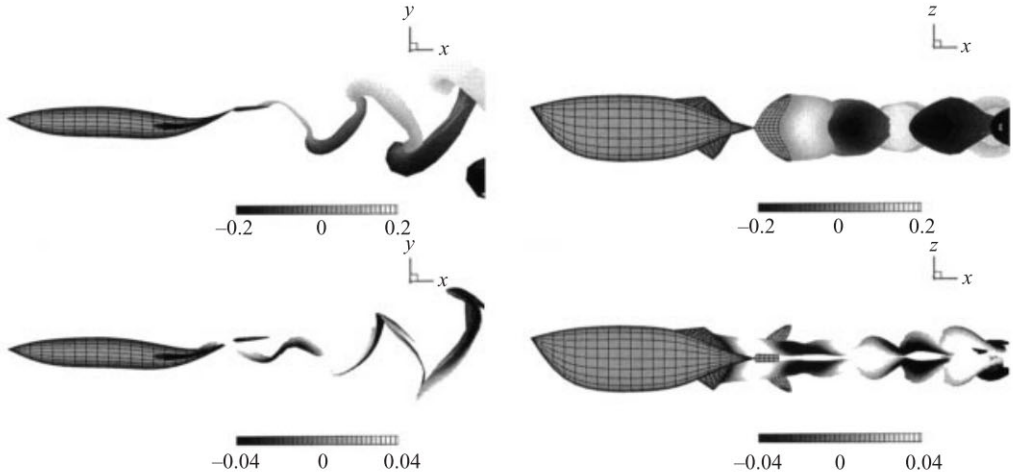


FIGURE 14. Formation of destructive mode in the wake of a straight-swimming giant danio at $t = 3T$. The top figures show the distribution of dipole strength on the tail-shed wake and the bottom figures show the distribution of dipole strength on the fin-shed wake. The dipole strength is normalized by UL . All of the kinematic parameters are as specified in §4.

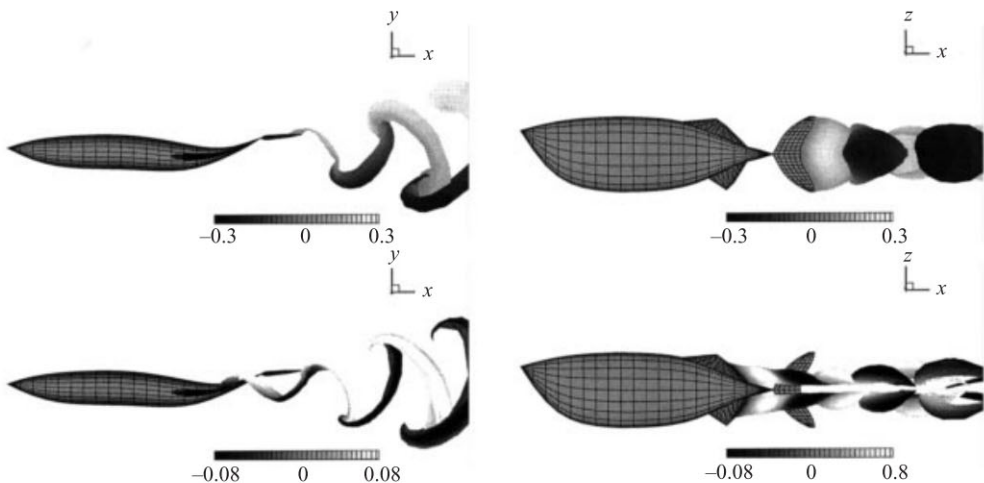


FIGURE 15. Formation of the constructive mode in the wake of a straight-swimming giant danio at $t = 3T$. The top figures show the distribution of dipole strength on the tail-shed wake and the bottom figures show the distribution of dipole strength on the fin-shed wake. The dipole strength is normalized by UL . Tailbeat frequency $f = 4.5$ Hz. All other kinematic parameters are identical to those specified in §4.

effect. In the present case, however, since the reverse Kármán vortex street caused by the tail is much stronger than the Kármán vortex street caused by the secondary fins, the flow downstream is still a jet-type wake.

By increasing the tailbeat frequency while keeping all other parameters unchanged, we also obtain a constructive vorticity interference case for the danio swimming. As illustrated in figure 15, the body-generated vorticity interacts constructively with the tail-shed vortices, strengthening the total reverse Kármán wake behind the fish.

6. Conclusions

The three-dimensional flow features of straight-line-swimming fish-like bodies are studied through a nonlinear, inviscid unsteady panel algorithm, allowing flow separation at the trailing edge of the caudal fin, as well as the trailing edges of a distribution of sharp finlets or secondary fins.

The flexing body is found to generate a three-dimensional flow which consists of a mixture of features characteristic of (a) the flow around a two-dimensional-flexing body, and (b) the dipole-like features assumed by slender body theory. Depending on the kinematic parameters, the near-body flow could be dominated by the two-dimensional features along much of the body, as in the case of a swimming tuna or it may be a mixture of these two features with the transverse flow increasing from head to tail, as in the case of a giant danio.

Our study also demonstrates the existence of two different modes of vorticity control employed by a straight-line-swimming fish to optimize performance by utilizing body-generated vortices. The constructive mode employs a vortex reinforcement scheme, whereby the oncoming body-generated vortices are repositioned and then paired with tail-generated same-sign vortices, resulting in a strong reverse Kármán street, and hence increased thrust force. The second mode, in contrast, employs a destructive interference scheme, whereby the oncoming body-generated vortices are repositioned and then paired with tail-generated opposite-sign vortices, resulting in a weakened reverse Kármán street, thus extracting energy from the oncoming body-shed vorticity and increasing swimming efficiency.

Financial support of the Office of Naval Research under contract N00014-99-1-1082 monitored by T. McMullen and P. Bandyopadhyay; the Defense Advanced Research Project Agency under contract DL-H-513308; and the Sea Grant Program under Grant Number NA46RG0434, is gratefully acknowledged.

REFERENCES

- ANDERSON, J. M. 1996 Vorticity control for efficient propulsion. Doctoral Thesis, Massachusetts Institute of Technology and the Woods Hole Oceanographic Institution.
- ANDERSON, J. M., STREITLIEN, K., BARRETT, D. S. & TRIANTAFYLLOU, M. S. 1998 Oscillating foils of high propulsive efficiency. *J. Fluid Mech.* **360**, 41–72.
- BARRETT, D. S. 1996 Propulsive efficiency of a flexible hull underwater vehicle. Doctoral Thesis, Massachusetts Institute of Technology, Cambridge, MA.
- BARRETT, D. S., TRIANTAFYLLOU, M. S., YUE, D. K. P., GROSENBAUGH, M. A. & WOLFGANG, M. 1999 Drag reduction in fish-like locomotion. *J. Fluid Mech.* **392**, 183–212.
- CHENG, J., ZHUANG, L. & TONG, B. 1991 Analysis of swimming of three-dimensional waving plates. *J. Fluid Mech.* **232**, 341–355.
- DEWAR, H. & GRAHAM, J. 1994 Studies of tropical tuna swimming performance in a large water tunnel. III. Kinematics. *J. Expl Biol.* **192**, 45–59.
- FFOWCS WILLIAMS, J. & ZHAO, B. 1989 The active control of vortex shedding. *J. Fluids Struct.* **3**, 115–122.
- FIERSTINE, H. & WALTERS, V. 1968 Studies in locomotion and anatomy of scombrid fishes. *Mem. Soc. South. Calif. Acad. Sci.* **6**, 1–31.
- GOPALKRISHNAN, R., TRIANTAFYLLOU, M., TRIANTAFYLLOU, G. & BARRETT, D. 1994 Active vorticity control in a shear flow using a flapping foil. *J. Fluid Mech.* **274**, 1–21.
- GRAY, J. 1936 Studies in animal locomotion: VI. The propulsive powers of the dolphin. *J. Expl Biol.* **13**, 192–199.
- GURSUL, I. & HO, C. 1992 High aerodynamic loads on an airfoil submerged in an unsteady stream. *AIAA J.* **30**, 1117–1119.
- KAGEMOTO, H., WOLFGANG, M., YUE, D. & TRIANTAFYLLOU, M. 2000 Force and power estimation

- in fish-like locomotion using a vortex-lattice method. *Trans. ASME: J. Fluids Engng* **122**(2), 239–253.
- KÁRMÁN, T. & BURGESS, J. M. 1935 General Aerodynamic theory – perfect fluids. In *Aerodynamic Theory*, Vol. II. Springer.
- KATZ, J. & PLOTKIN, A. 1991 *Low-speed Aerodynamics: from Wing Theory to Panel Methods*. McGraw-Hill.
- KOOCHESFAHANI, M. & DIMOTAKIS, P. 1988 A cancellation experiment in a forced turbulent shear layer. *AIAA Tech. Paper* 88-3713-CP.
- KRASNY, R. 1986 Desingularization of periodic vortex sheet roll-up. *J. Comput. Phys.* **65**, 292–313.
- LAN, C. 1979 The unsteady quasi-vortex-lattice method with applications to animal propulsion. *J. Fluid Mech.* **93**, 747–765.
- LIGHTHILL, M. 1960 Note on the swimming of slender fish. *J. Fluid Mech.* **9**, 305–317.
- LIGHTHILL, M. 1970 Aquatic animal propulsion of high hydromechanical efficiency. *J. Fluid Mech.* **44**, 265–301.
- LIGHTHILL, M. 1971 Large amplitude elongated-body theory of fish locomotion. *Proc. R. Soc. Lond. B* **179**, 125–138.
- LIGHTHILL, M. 1975 *Mathematical Biofluidynamics*. SIAM.
- LIU, H., WASSENBERG, R. & KAWACHI, K. 1997 The three-dimensional hydrodynamics of tadpole swimming. *J. Expl Biol.* **200**, 2807–2819.
- MÜLLER, U., VAN DEN HEUVEL, B., STAMHUIS, E. & VIDELER, J. J. 1997 Fish foot prints: Morphology and energetics of the wake behind a continuously swimming mullet (*Chelon Labrosus Risso*). *J. Expl Biol.* **200**, 2893–2906.
- NEWMAN, J. 1973 The force on a slender fish-like body. *J. Fluid Mech.* **58**, 689–702.
- NEWMAN, J. & WU, T. 1973 A generalized slender-body theory for fish-like forms. *J. Fluid Mech.* **57**, 673–693.
- PEDLEY, T. J. & HILL, S. J. 1999 Large-amplitude undulatory fish swimming: Fluid mechanics coupled to internal mechanics. *J. Expl Biol.* **202**, 3431–3438.
- ROHR, J., HENDRICKS, E., QUIGLEY, L., FISH, F., GIPATRICK, J. & SCARDINA-LUDWIG, J. 1998 Observations of dolphin swimming speed and Strouhal number. *Space and Naval Warfare Systems Center, Tech. Rep.* 1769, San Diego, CA.
- ROSEN, M. 1959 Water flow about a swimming fish. *United States Naval Ordnance Test Station, NAVWEPS Rep.* 2298, China Lake, CA.
- STAMHUIS, E. & VIDELER, J. J. 1995 Quantitative flow analysis around aquatic animals using laser sheet particle image velocimetry. *J. Expl Biol.* **198**, 283–294.
- STREITLIEN, K. & TRIANTAFYLLOU, G. 1998 On thrust estimates for flapping foils. *J. Fluids Struct.* **12**, 47–55.
- STREITLIEN, K., TRIANTAFYLLOU, G. & TRIANTAFYLLOU, M. 1996 Efficient foil propulsion through vortex control. *AIAA J.* **34**, 2315–2319.
- TOKOMARU, P. & DIMOTAKIS, P. 1991 Rotary oscillation control of a cylinder wake. *J. Fluid Mech.* **224**, 77–90.
- TRIANTAFYLLOU, M. S., TRIANTAFYLLOU, G. S. & GOPALKRISHNAN, R. 1991 Wake mechanics for thrust generation in oscillating foils. *Phys. Fluids A* **3**, 2835–2837.
- TRIANTAFYLLOU, G. S., TRIANTAFYLLOU, M. S. & GROSENBAUGH, M. A. 1993 Optimal thrust development in oscillating foils with application to fish propulsion. *J. Fluids Struct.* **7**, 205–224.
- TRIANTAFYLLOU, G., TRIANTAFYLLOU, M. & YUE, D. K. P. 2000. Hydrodynamics of Fish Swimming. *Annu. Rev. Fluid Mech.* **32**, 33–53.
- TRIANTAFYLLOU, M. S., BARRETT, D. S., YUE, D. K. P., ANDERSON, J. M., GROSENBAUGH, M. A., STREITLIEN, K. & TRIANTAFYLLOU, G. S. 1996 A new paradigm of propulsion and maneuvering for marine vehicles. *Trans. Soc. Naval Archit. Mar. Engrs* **104**, 81–100.
- VIDELER, J. J., MULLER, U. K. & STAMHUIS, E. J. 1999 Aquatic vertebrate locomotion: Wakes from body waves. *J. Expl Biol.* **202**, 3423–3430.
- WOLFGANG, M. 1999 Hydrodynamics of flexible-body swimming motions. Doctoral Thesis, Massachusetts Institute of Technology, Cambridge, MA.
- WOLFGANG, M., ANDERSON, J. M., GROSENBAUGH, M. A., YUE, D. K. P. & TRIANTAFYLLOU, M. S. 1999a Near-body flow dynamics in swimming fish. *J. Expl Biol.* **202**, 2303–2327.
- WOLFGANG, M., TRIANTAFYLLOU, M. S. & YUE, D. K. P. 1999b Visualization of complex near-body transport processes in flexible-body propulsion. *J. Visualization* **2**, 143–151.

- WU, T. 1961 Swimming of waving plate. *J. Fluid Mech.* **10**, 321–344.
- WU, T. 1971a Hydromechanics of swimming propulsion. Part 1. Swimming of a two dimensional flexible plate at variable forward speeds in an inviscid fluid. *J. Fluid Mech.* **46**, 337–355.
- WU, T. 1971b Hydromechanics of swimming propulsion. Part 2. Some optimum shape problems. *J. Fluid Mech.* **46**, 521–544.
- WU, T. 1971c Hydromechanics of swimming propulsion. Part 3. Swimming and optimum movements of slender fish with side fins. *J. Fluid Mech.* **46**, 545–568.